Supporting Information

Uncovering the Role of Organic Species in SEI on graphite Towards Fast K^+ Transport and Long-life Potassium-ion Batteries

Ying Mo [a#], *Wang Zhou* [a#], *Kexuan Wang* [b], *Wenwen Yang* [a], *Zixu Liu* [a], *Shi Chen* [b],

Peng Gao [a,c,] *, *Jilei Liu*[a,] *

[a] *College of Materials Science and Engineering, Hunan Joint International Laboratory of Advanced Materials and Technology of Clean Energy, Hunan Province Key Laboratory for Advanced Carbon Materials and Applied Technology, Hunan University, Changsha, 410082, China*

[b] *Joint Key Laboratory of the Ministry of Education, Institute of Applied Physics and Materials Engineering, University of Macau, Macau, 999078, China*

[c] *Greater Bay Area Institute for Innovation, Hunan University, Guangzhou 511300, China*

* *Corresponding Authors. E-mail: gaop@hnu.edu.cn; liujilei@hnu.edu.cn*

[#] *Y. Mo and W. Zhou contributed equally to this work.*

Experimental Section

Electrode preparation and solid electrolyte interphases (SEI) chemistry regulation.

Graphite anodes: the graphite (Gr) anodes were prepared with commercial graphite (80 wt.%), kejten black (10 wt.%) and sodium alginate (10 wt.%), all these powders were mixed and stirred in deionized water for 8 h to get a homogeneous slurry. In which, the kejten black and sodium alginate were purchased from Canrd Technology Co. Ltd.. Then, the slurry was coated on copper foil, and the 14 mm discs electrodes were obtained after dried at 80ºC for 12 h in vacuum. The mass loading of the as-prepared graphite anodes is 0.95-1.0 mg cm^{-2}.

Prussian white cathodes: KFeHCF was obtained by a typical co-precipitation method. KFeHCF powder (70 wt.%), super P (20 wt.%) and polyvinylidene fluoride (PVDF, provided by Energy Chemical) (10 wt.%) in N-methylpyrrolidone (NMP, provided by Adamas-beta) were stirred for 8 h to form a slurry. After being coated on an aluminum foil and dried at 110ºC for 12 h in vacuum, it was cut into 12 mm discs for further use. The mass loading of the cathode electrodes is 1.7-1.9 mg cm^{-2}.

SEI chemistry regulation**:** For better understanding the role of SEI’s organic and inorganic components on graphite in determining electrochemical performance of PIBs, the compositions of full cell were kept same except the SEI properties. In which, the SEI chemistry regulation was based on half cell electrochemical method (HC-EM) by using CR2032-type coin cells (supplied by Canrd Technology Co. Ltd.) assembled in an argon filled glove box with oxygen and water contents below 0.01 ppm. The coin cells were tested on LAND CT2001A battery testing system and Neware battery test system (CT-4008T). In order to modify the SEI chemistry, Gr/K half cells were cycled at various temperatures, while KFeHCF/K half cells were exclusively cycled at 25ºC. Each coin cell underwent 3 times for the sufficient formation of electrode/electrolyte interphase by using 0.8 M KPF_6 in EC: DEC, where the Gr anodes were cycled between 0.01-3.0 V at 0.05 C (1 C= 279 mA g^{-1}), and KFeHCF cathodes were cycled between 2.0-4.5 V at 0.1 C, (1 C= 100 mA g^{-1}). Then these coin cells were disassembled for full cells. The KFeHCF/Gr full cells were assembled using Whatman glass fiber separator and 0.8 M KPF_6 in EC: DEC as the electrolyte for further electrochemical experiments, the N/P value was determined to be around 1.1. For cyclic and rate performances, these KFeHCF/Gr full cells were first charged to 4.5 V at a constant current (CC) rate, followed by constant voltage (CV) mode until the current rate decreased to less than 0.05 C (1 C = 100 mA g^{-1}), and then were discharged to 2.0 V with CC mode. All calculations are based on the mass of cathode electrode. Galvanostatic Intermittent Titration Technique (GITT) was also performed on a battery test system after three standard cycles at 20 mA g^{-1}. The diffusion coefficients are calculated based on the cathode. Electrochemical impedance spectroscopy (EIS) measurements were performed in the frequency range from 0.1 Hz-100 kHz with 10 mV oscillation amplitude on Solartron system. All EIS data subtract the part where frequencies are less than 0.1 Hz, and obey Kramers-Kronig relations. The distribution of relaxation time (DRT) analysis has been used to separate different polarization processes, which is obtained by transforming the EIS data from frequency domain to time domain. The activation energies (E_A) of the charge transfers and K^+ across SEI were obtained by EIS measurements at several temperatures, based on the following equation (1):

$$\frac{1}{R_{ct/SEI}} = c \cdot e^{\frac{-E_A}{RT}} \tag{1}$$

Where $R_{ct/SEI}$ is resistance, c is the constant, E_A is activation energy, R is universal gas constant, and T is absolute temperature.

In situ FT-IR Measurement: In situ FT-IR experiments were conducted in an electrochemical cell having two electrodes. The spectra of samples were collected using Nicolet iS50 (Thermo Fisher Scientific) with a mercury cadmium telluride (MCT) detector, all spectra were acquired with a resolution of 4 cm^{-1} and a total of 64 scans. A Si crystal was used as IR window which provides a reliable signal above 1100 cm^{-1}. The spectra of selected potential were carried out to examine the SEI formation. Typically, the negative and positive peaks correspond to the vibration of degradation species and newly formed species.

XPS Measurement: The cycled electrodes were opened inside the glovebox and rinsed with dimethyl carbonate (DMC, ≥ 99 %). The DMC possesses advantages, such as low boiling point, low viscosity, high surface tension, good solubility for electrolyte salts, and hardly changes the SEI compositions. A monochromatic X-ray source (Al *Kα*, *hυ* = 1486.7 eV) was used for XPS in ultrahigh-vacuum (UHV) chamber. The low energy Ar^+ clusters (2000 eV) were used to prevent chemical damage to the underlying material. C1s-K 2p, O 1s and F 1s X-ray photoelectron spectra were calibrated by setting the binding energy for the hydrocarbon (C-C/C-H) in C 1s spectra to 285 eV.

Raman Measurement: Raman mappings were performed using WITEC alpha 300R Raman system (532 nm laser). Each spectrum of mapping with acquisition times of 10 s, once. The temperature-dependent Raman spectroscopy of electrolyte were carried out on HCP421V-MPS Micro Probing Station under different temperatures.

BET Measurement: The Branauer–Emmett–Teller (BET) specific surface area was obtained via nitrogen adsorption-desorption isotherms (JW-BK200C, Beijing JWGB SCI & TECH).

XRD Measurement: The X-ray diffraction (XRD) patterns for samples were measured using an X-ray diffractometer (Rigaku Miniflex 600, KW-ST Lab (https://www.kewei-scitech.com)) with Cu Kα radiation (λ = 1.5418 Å).

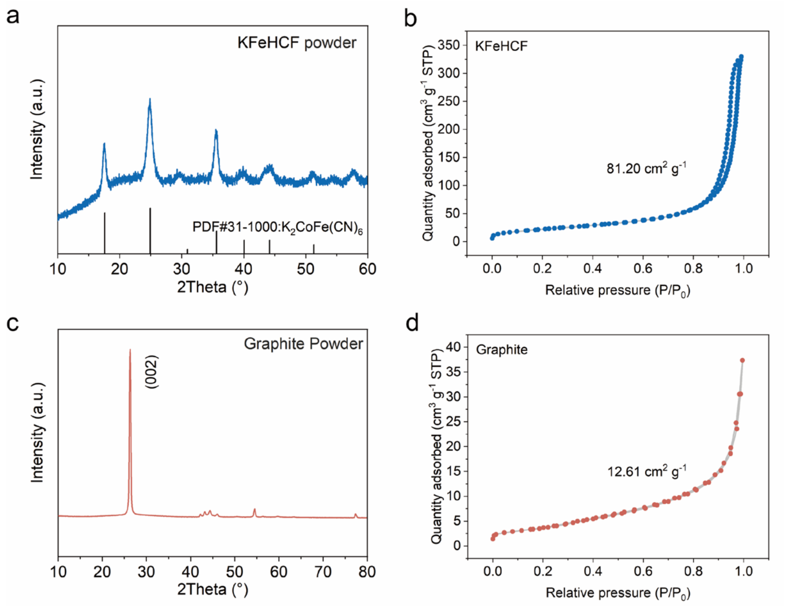

Figure S1. The structural characterizations of KFeHCF and graphite: (a) XRD patterns and (b) N_2 adsorption-desorption isotherm of KFeHCF, (c) XRD patterns and (d) N_2 adsorption-desorption isotherm of graphite.

Supplementary Note 1:

Figure S1a shows the XRD pattern of KFeHCF synthesized via the co-precipitation method. All peaks are corresponding well to the standard diffraction pattern of $K_2CoFe(CN)_6$, as referenced in the PDF Card No. 31-1000, confirming the formation of a pure phase. The specific surface area for the as-prepared KFeHCF sample is 81.20 cm^2 g^{-1} (**Figure S1b**). **Figure S1c** shows the XRD pattern for graphite. The XRD peaks at 26.32°, 44.36° and 54.48° are corresponding to the (002), (101) and (004) planes, respectively. The specific surface area for the graphite sample is 12.61 cm^2 g^{-1} (**Figure S1d**).

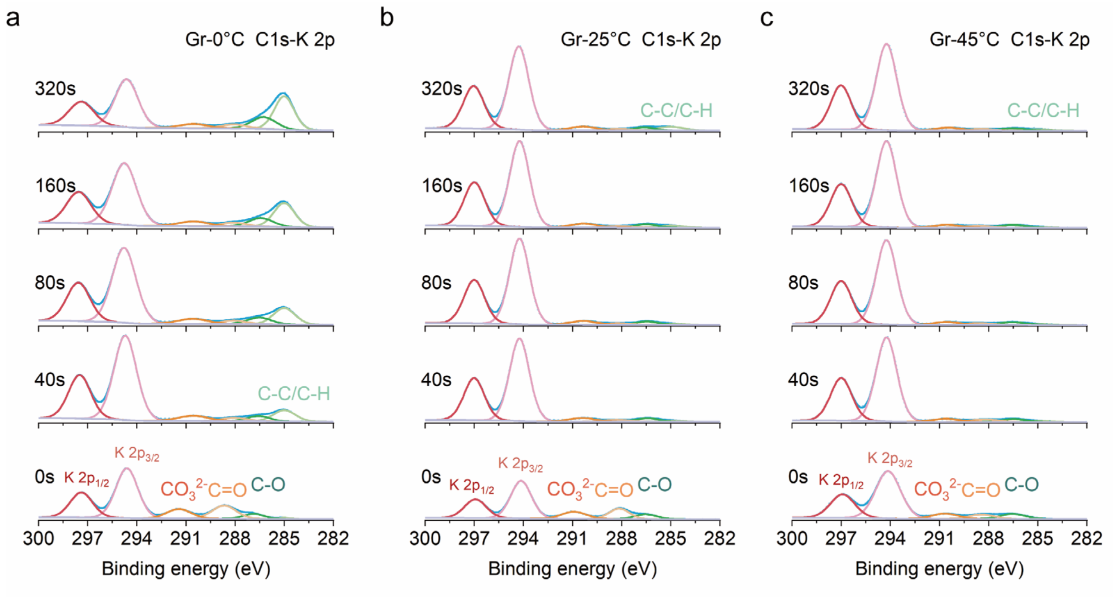

Figure S2. Comparative C 1s-K 2p spectra retrieved from Gr/K half cells after 3 cycles of SEI formation at 0.01 V with different Ar^+ bombardment times: (a) Gr-0°C, (b) Gr-25°C, (c) Gr-45°C.

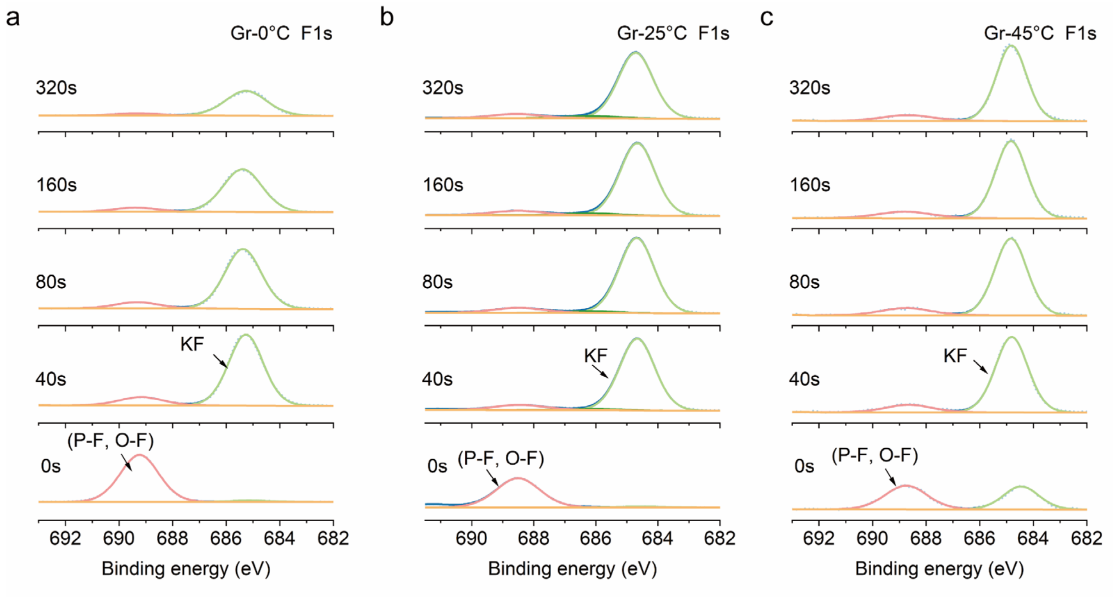

Figure S3. Comparative F 1s spectra retrieved from Gr/K half cells after 3 cycles of SEI formation at 0.01 V with different Ar^+ bombardment times: (a) Gr-0°C, (b) Gr-25°C, (c) Gr-45°C.

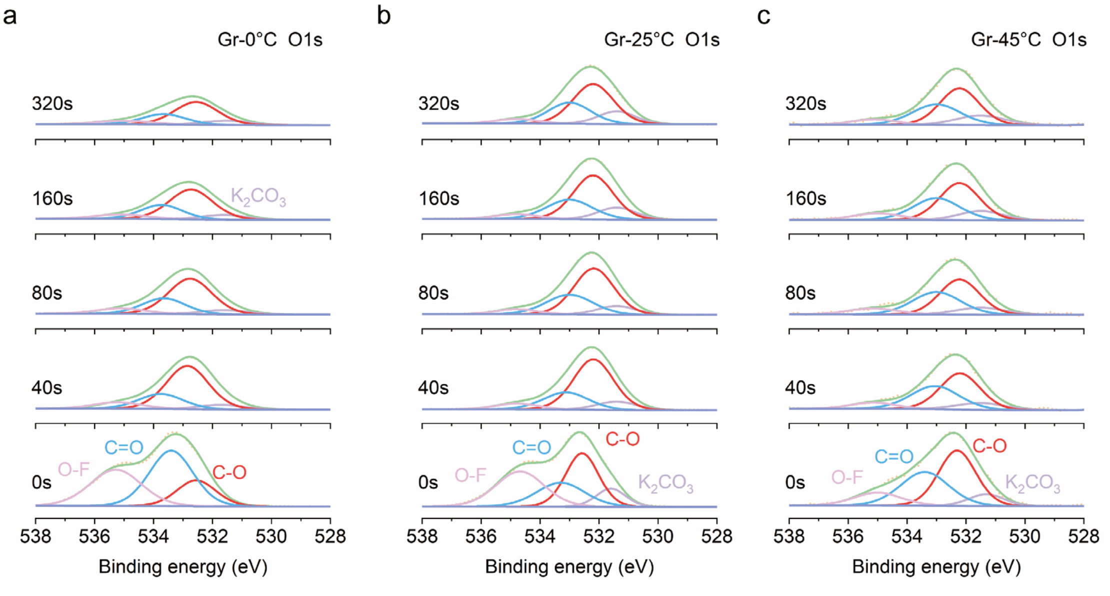

Figure S4. Comparative O 1s spectra retrieved from Gr/K half cells after 3 cycles of SEI formation at 0.01 V with different Ar$^+$ bombardment times: (a) Gr-0°C, (b) Gr-25°C, (c) Gr-45°C with different Ar$^+$ bombardment times.

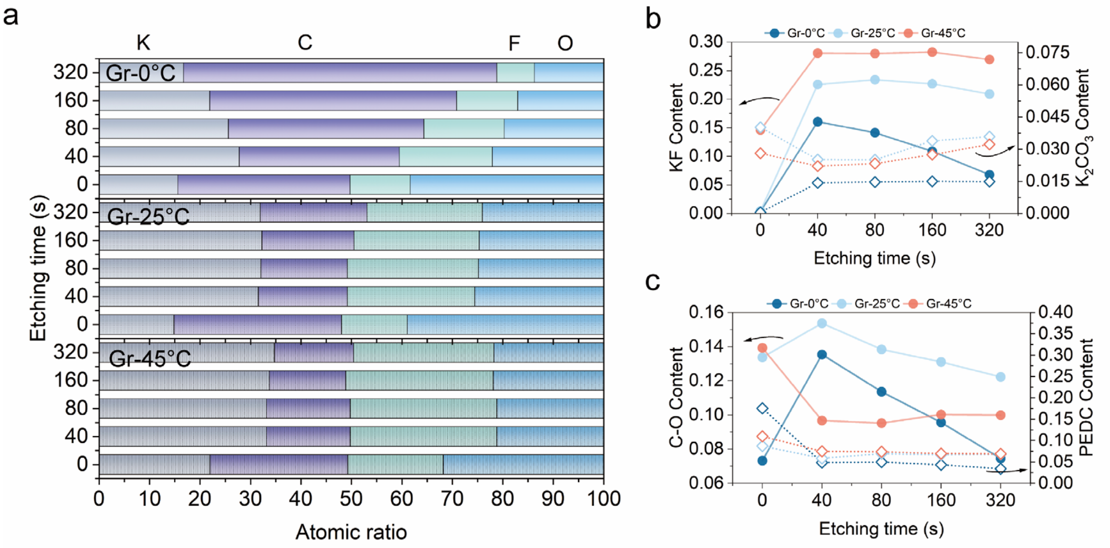

Figure S5 (a) Composition of SEI measured by XPS depth-profiling retrieved from Gr/K half cells after 3 cycles of SEI formation at 0.01 V with sputtering time from 0 s to 320 s, (b) inorganic components within the SEI (KF based on F 1s, K_2CO_3 based on O 1s), (c) organic components within the SEI (C-O based on O 1s, PEDC based on O 1s).

Supplementary Note 2:

The C 1s spectra of SEI shown in **Figure S2** can be deconvoluted into five peaks include C-C/C-H (~285 eV), C-O (~286.4 eV), C=O (~288.3 eV) and CO_3^{2-} (~290.4 eV). The C-C/C-H bonds could be ascribed to graphite/or kejten black in the electrode, the C-O, C=O and CO_3^{2-} bonds are originated from organic and inorganic species such as polyether/oligo-oxygen/(-$(CH_2CH_2O)_n$- (PEO)), potassium ethylene decarbonate (RO-CO_2K (PEDC)) and potassium carbonate (K_2CO_3).[1] The strong C-C peak observed throughout the sputtering time demonstrating that the as-formed SEI of Gr-0°C is very thin. Two peaks centered at 684.8 and 688.7 eV in F 1s spectra are assigned to K-F and O-F/P-F bonds (**Figure S3**). The K-F bond is related to KF that is formed from KPF_6 decomposition. The O-F/P-F bonds are corresponding to $K_xPF_yO_z$ and K_xPF_y which are formed by incomplete KPF_6 decomposition.[2] Four peaks centered at 531.5, 532.2, 533.2 and 535.1 eV in O 1s spectra are attributed to CO_3^{2-}, C-O, C=O and O-F bonds, which are mainly originated from K_2CO_3, PEO, PEDC and $K_xPF_yO_z$ (**Figure S4**). The PEDC and $K_xPF_yO_z$ are mainly accumulated in the outer layer, the K_2CO_3 is mainly reside in the inner layer, and the PEO is evenly distributed throughout the CEI layer, a feature that is consistent with the common mosaic structure model.[3] The electrolyte decomposition and conversion reactions between different components can be expressed as follows[2, 4, 5]:

$$2(CH_2O)_2CO + 2K^+ + 2e^- \rightarrow (CH_2OCO_2K)_2 + C_2H_4 \qquad (2)$$

$$(CH_2O)_2CO + 2K^+ + 2e^- \rightarrow K_2CO_3 + C_2H_4 \qquad (3)$$

$$n(CH_2O)_2CO \xrightarrow{PF_5,RO^-} (-CH_2CH_2O-)_n + nCO_2 \qquad (4)$$

$$2CH_3CH_2OCO_2K + H_2O \rightarrow K_2CO_3 \downarrow + 2CH_3CH_2OH + CO_2 \uparrow \qquad (5)$$

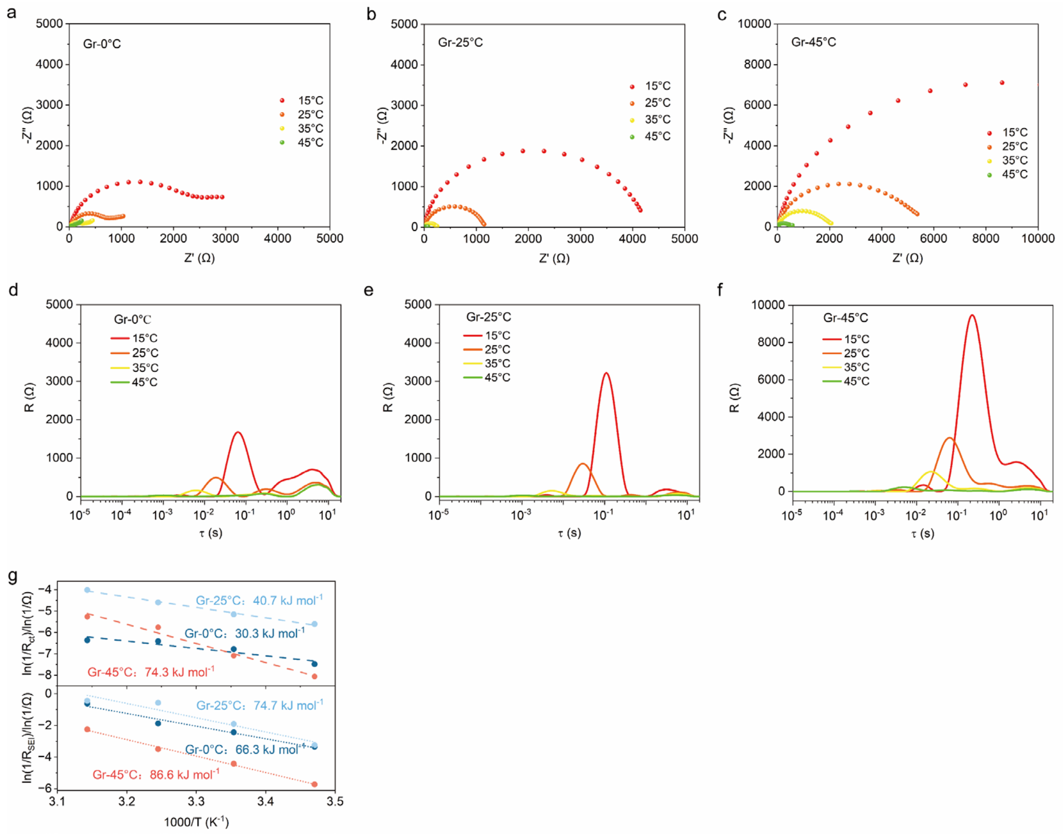

Figure S6. Nyquist impedance spectroscopy at a Gr/K half cells voltage of 0.01 V in different temperatures (15, 25, 35, 45ºC, the absolute temperature are 288.15, 298.15, 308.15, 318.15 K, respectively): (a) 0°C, (b) 25°C, (c) 45°C. The corresponding DRT results: (d) 0°C, (e) 25°C, (f) 45°C. (g) Activation energies of R_{ct} and R_{SEI} at about 0.01 V for different cells.

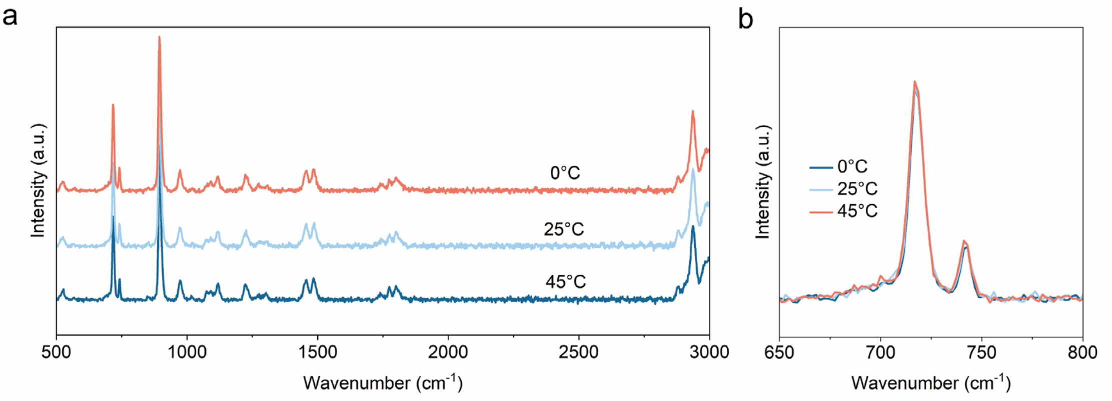

Figure S7. Temperature-dependent Raman test: (a) Raman spectra of electrolyte at different temperature, (b) The corresponding enlarged part of Raman spectra in the range of 650 to 800 cm^{-1}, the peak at approximately 745 cm^{-1} is attributed to the P-F vibration of PF_6^-.

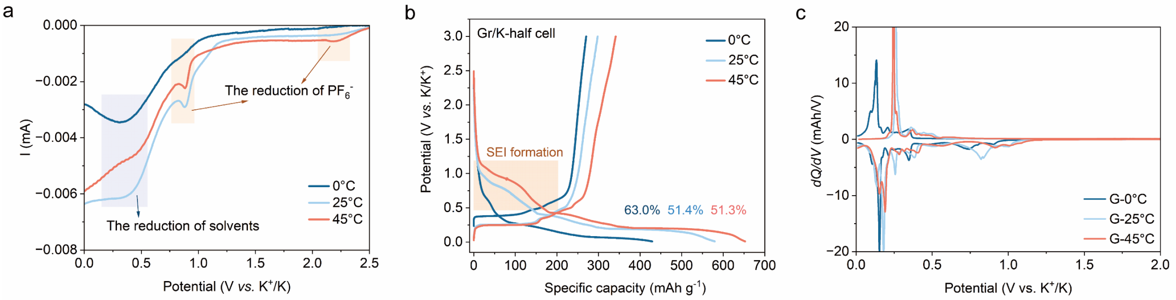

Figure S8. (a) Linear scan voltammetry curves of K/stainless steel in electrolytes. (b) 1st charge-discharge curves of Gr/K half cells. (c) dQ/dV profiles of Gr/K half cells.

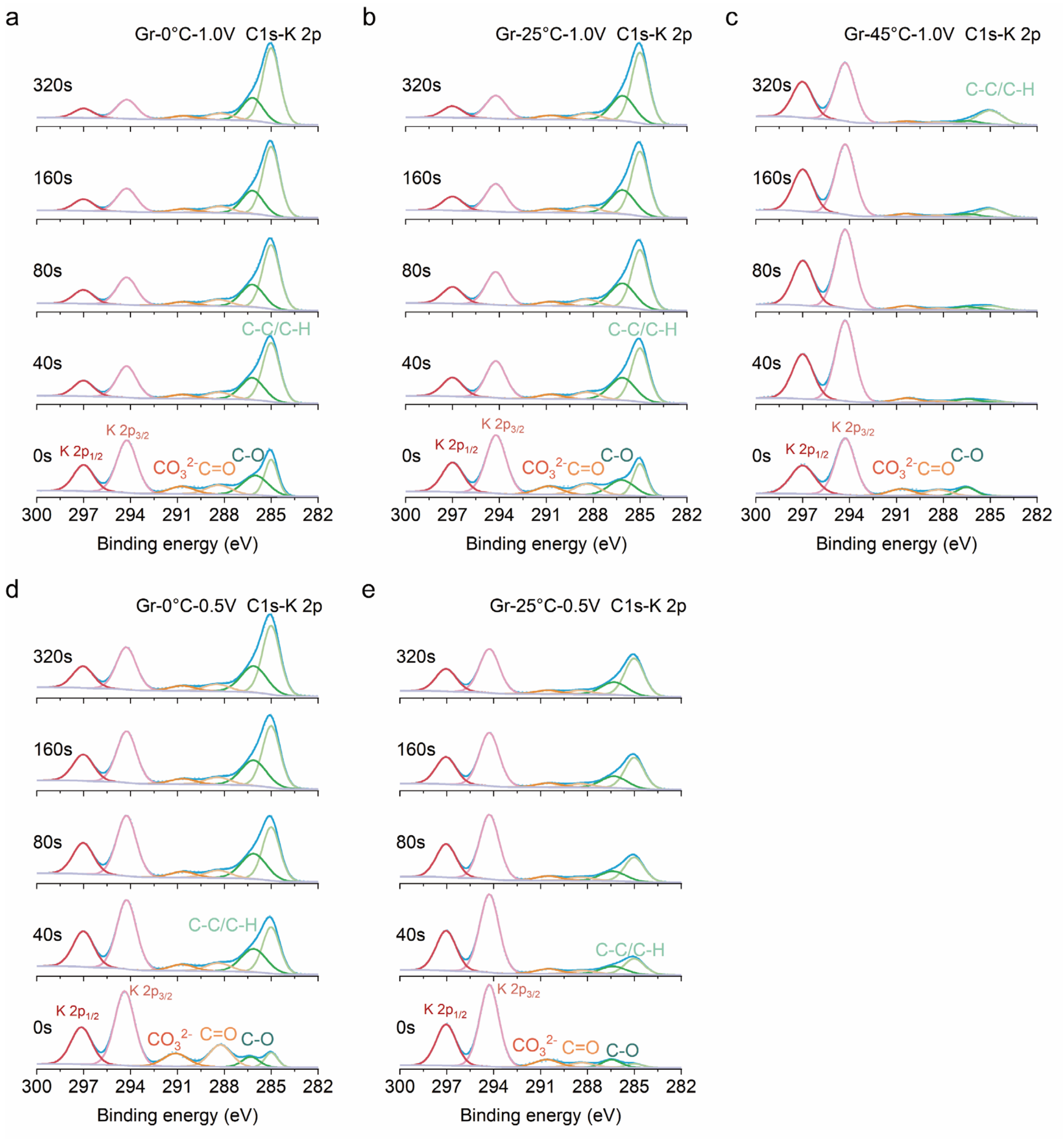

Figure S9. Comparative C 1s-K 2p spectra of (a) Gr-0°C-1.0 V, (b) Gr-25°C-1.0 V, (c) Gr-45°C-1.0 V, (d) Gr-0°C-0.5 V, (e) Gr-25°C-0.5 V with different Ar^+ bombardment times.

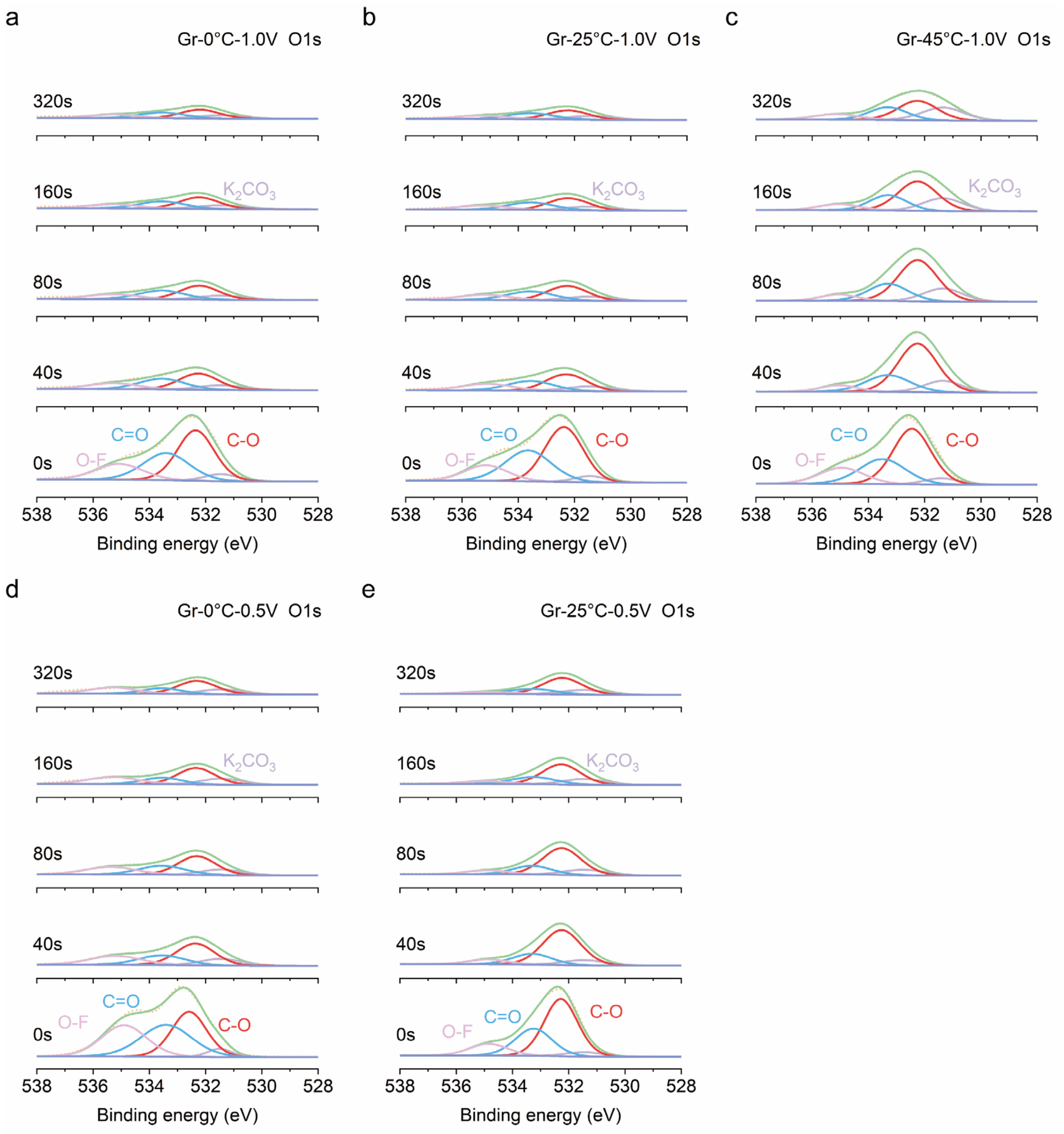

Figure S10. Comparative O 1s spectra of (a) Gr-0°C-1.0 V, (b) Gr-25°C-1.0 V, (c) Gr-45°C-1.0 V, (d) Gr-0°C-0.5 V, (e) Gr-25°C-0.5 V with different Ar^+ bombardment times.

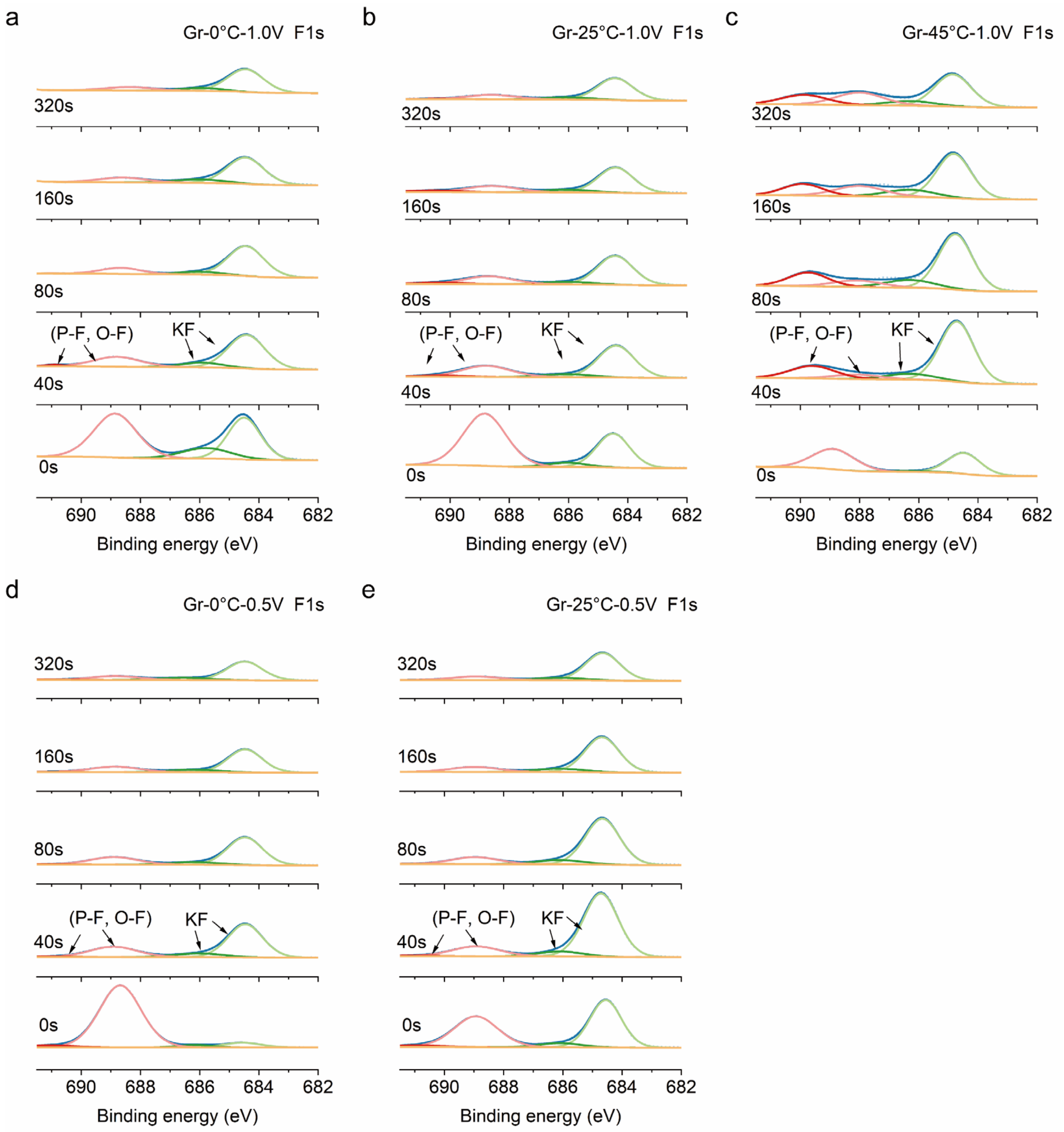

Figure S11. Comparative F 1s spectra of (a) Gr-0°C-1.0 V, (b) Gr-25°C-1.0 V, (c) Gr-45°C-1.0 V, (d) Gr-0°C-0.5 V, (e) Gr-25°C-0.5 V with different Ar^+ bombardment times.

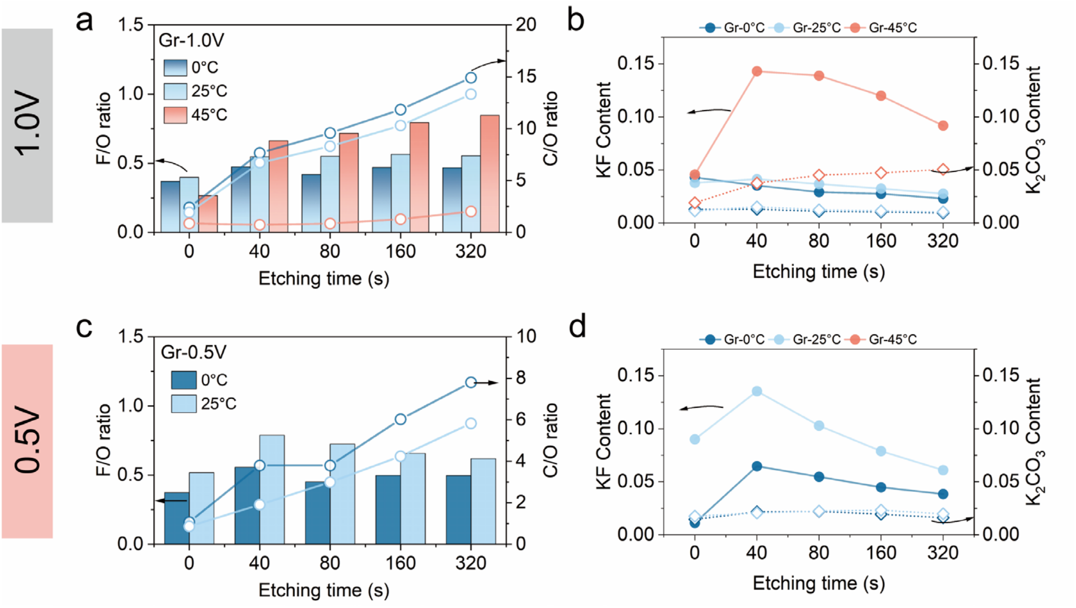

Figure S12. (a) Relative atomic ratios of F/O and C/O at 1.0 V, (b) inorganic components (KF based on F 1s, K_2CO_3 based on O 1s) at 1.0 V, (c) Relative atomic ratios of F/O and C/O at 0.5 V, (d) inorganic components (KF based on F 1s, K_2CO_3 based on O 1s) at 0.5 V.

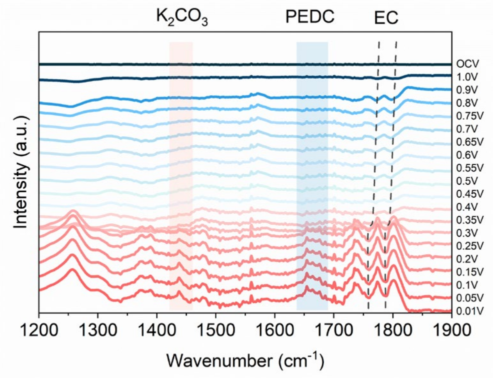

Figure S13. In situ FTIR characterization on the formation of SEI at 25°C.

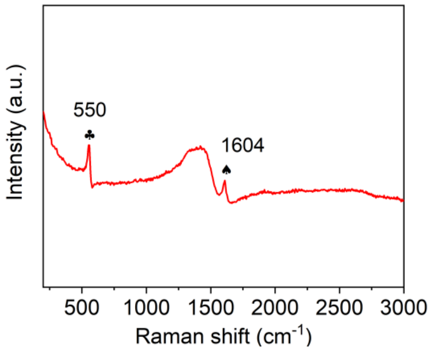

Figure S14. Raman spectra of the graphite electrode in Gr/K half cell discharged to 0.01 V.

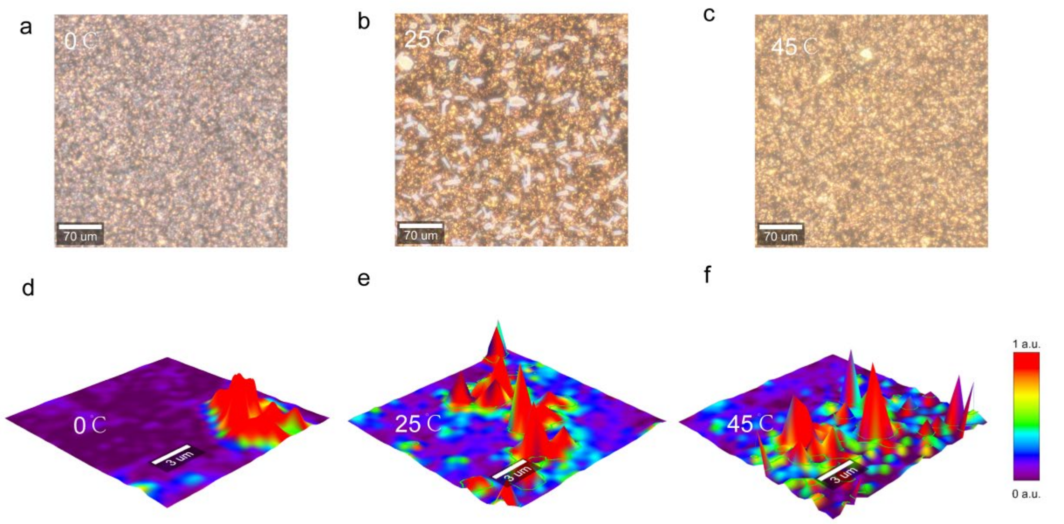

Figure S15. The optical images of the graphite electrode in Gr/K half cells discharged to 0.01 V: (a) Gr-0°C, (b) Gr-25°C, and (c) Gr-45°C. The Raman mapping results of the graphite electrode in Gr/K half cells discharged to 0.01 V: (d) Gr-0°C, (e) Gr-25°C, and (f) Gr-45°C.

Supplementary Note 3:

Raman spectroscopy can monitor the electrochemically driven phase transition process of K-GIC. According to previous studies, upon discharging the graphite anode to 0.3 V, a new characteristic peak emerges at approximately 1600 cm^{-1} near the G peak (1580 cm^{-1}), indicating the formation of GIC (graphite intercalation compound). As the K^+-intercalation proceeds, the intensity of the peak at approximately 1600 cm^{-1} increases. Furthermore, the peak at approximately 560 cm^{-1} is the characteristic peak of KC_8[6]. **Figure S14** shows the Raman spectra of the graphite electrode in Gr/K half cells discharged to 0.01 V, indicating that the graphite is in a state of coexistence between stage 2 (KC_{24}/KC_{16}) and stage 1 (KC_8)[7].

Raman spectroscopic imaging technology was further employed to investigate the influence of cycling at various temperatures on the kinetic behavior of graphite anode.

Figure S15a-c show the optical images of the graphite electrodes at different temperatures after being discharged to 0.01 V, respectively. It is evident that the electrodes exhibit a golden yellow color, indicative of the formation of KC_8, and the intensity of the golden hue increases with the elevation of temperature.

Raman mapping further corroborated the aforementioned conclusions. By utilizing the ratio of the peak area at 550 cm^{-1} to that at 1600 cm^{-1}, the proportion of KC_8 (stage 1) in different graphite electrodes can be characterized. **Figure S15d-f** show the Raman mapping results for graphite electrodes discharged to 0.01 V at various temperatures, respectively. With the increase in temperature, the proportion of KC_8 in the graphite electrodes increases and is more uniformly distributed.

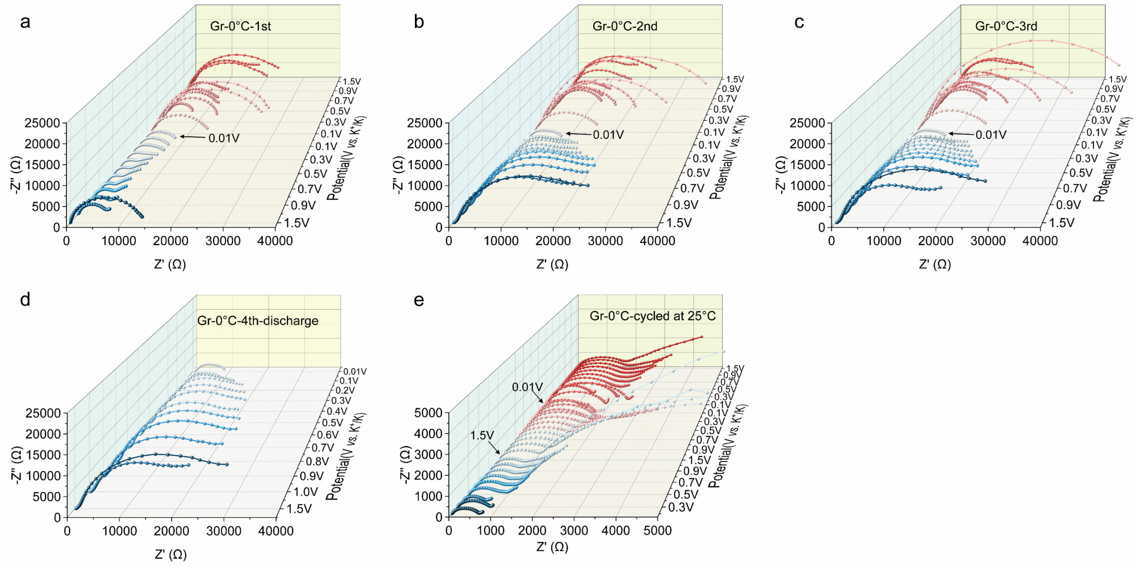

Figure S16. In situ EIS of Gr/K half cell at 0°C: (a) 1st cycle, (b) 2nd cycle, (c) 3rd cycle, and (d) 4th cycle, (e) Gr-0°C cycled at 25°C.

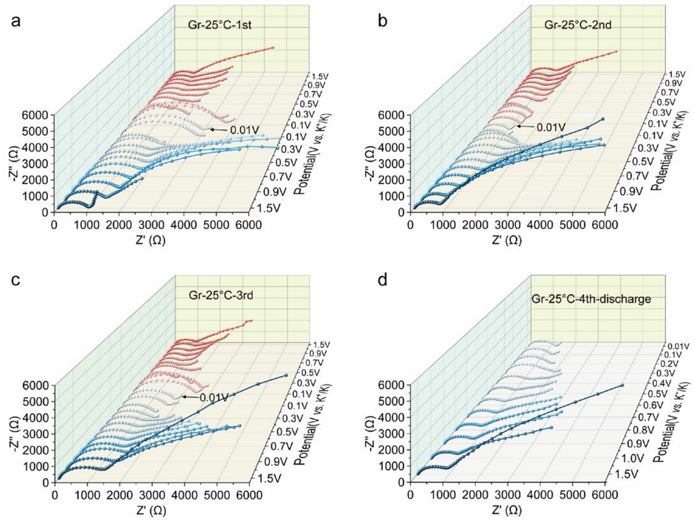

Figure S17. In situ EIS of Gr/K half cell at 25°C: (a) 1st cycle, (b) 2nd cycle, (c) 3rd cycle, and (d) 4th cycle.

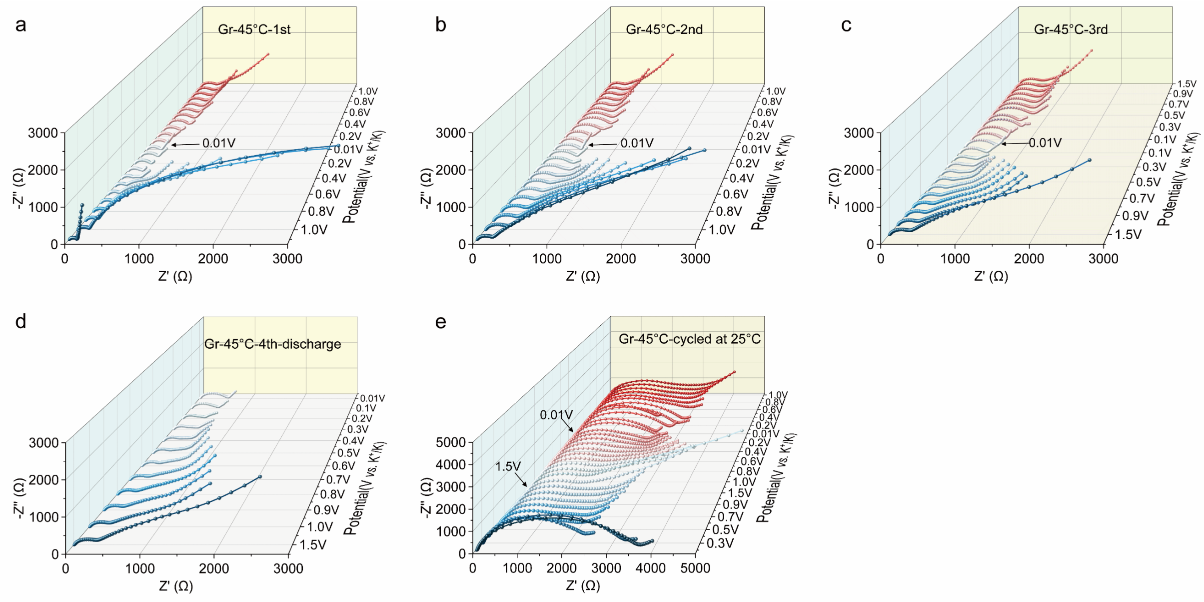

Figure S18. In situ EIS of Gr/K half cell at 45°C: (a) 1st cycle, (b) 2nd cycle, (c) 3rd cycle, and (d) 4th cycle, (e) Gr-45°C cycled at 25°C.

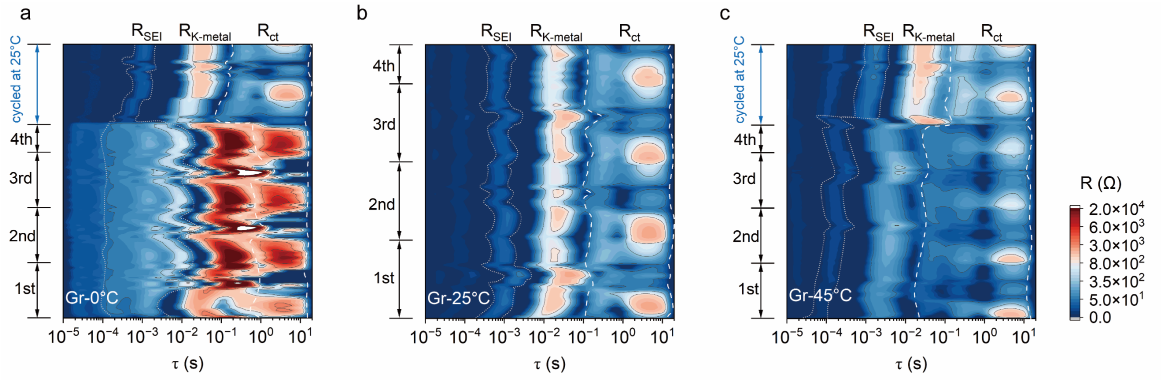

Figure S19. DRT results of Gr/K half cells at various temperatures: (a) 0°C, (b) 25°C, (c) 45°C.

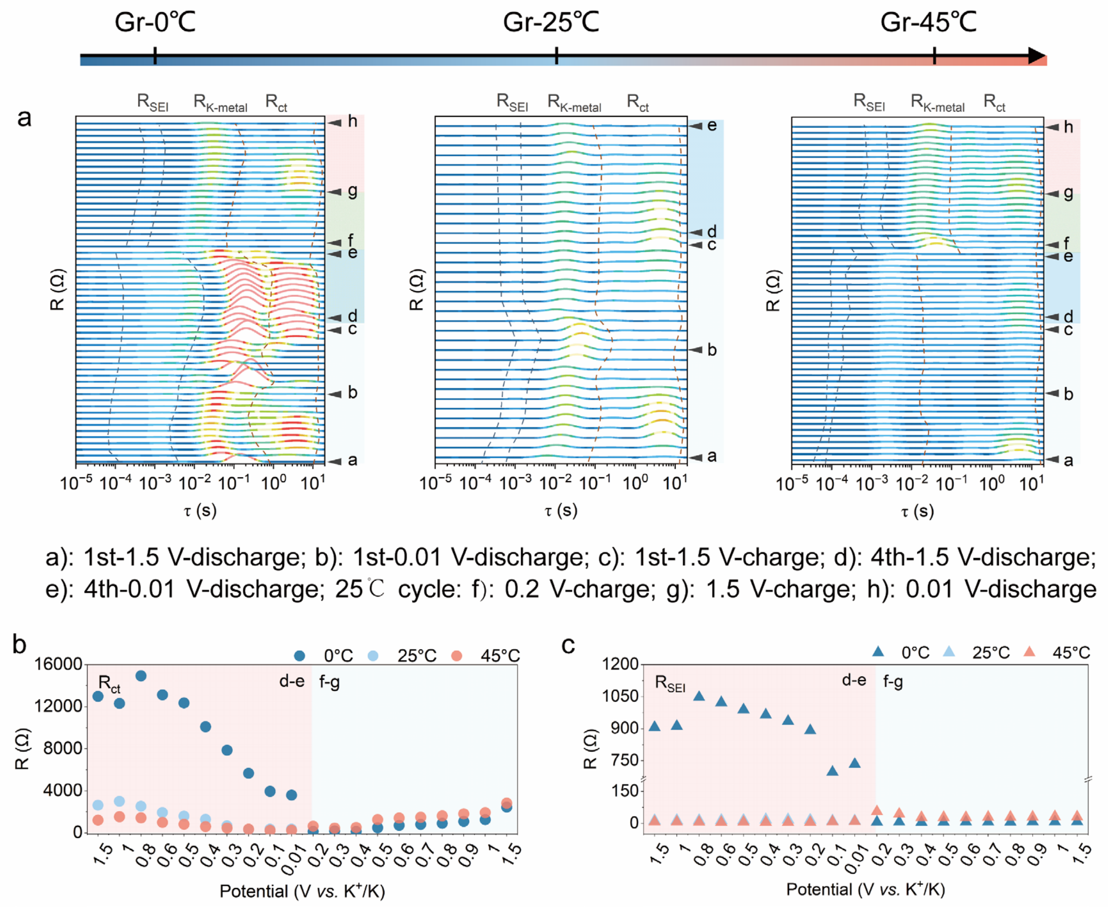

a): 1st-1.5 V-discharge; b): 1st-0.01 V-discharge; c): 1st-1.5 V-charge; d): 4th-1.5 V-discharge; e): 4th-0.01 V-discharge; 25℃ cycle: f): 0.2 V-charge; g): 1.5 V-charge; h): 0.01 V-discharge

Figure S20. (a) DRT results of Gr/K half cells at various temperatures. Fitting resistance versus voltage profiles based on DRT results for (b) R_{ct}, and (c) R_{SEI}.

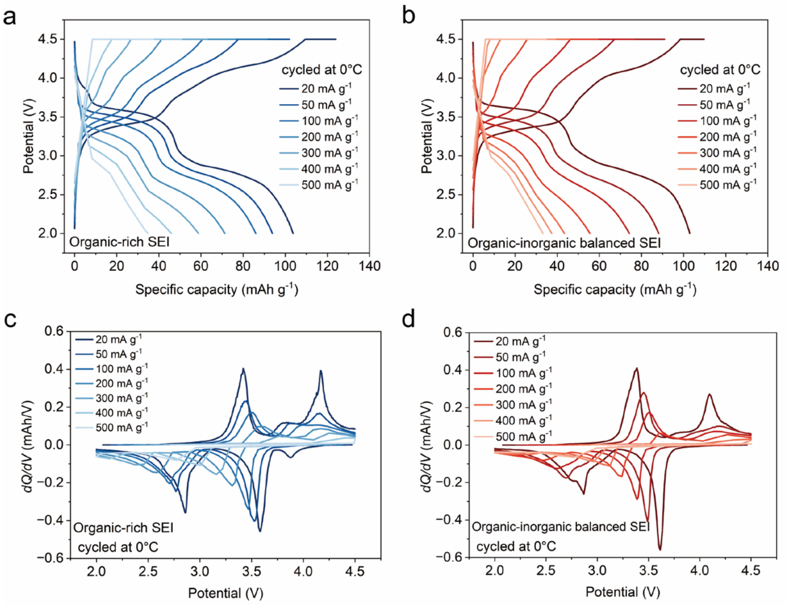

Figure S21. Charge-discharge curves of KFeHCF/Gr full cells at different current densities, cycled at 0°C: (a) Organic-rich SEI, (b) Organic-inorganic balanced SEI. Differential capacity (dQ/dV) profiles of KFeHCF/Gr full cells at different current densities, cycled at 0°C: (c) Organic-rich SEI, (d) Organic-inorganic balanced SEI.

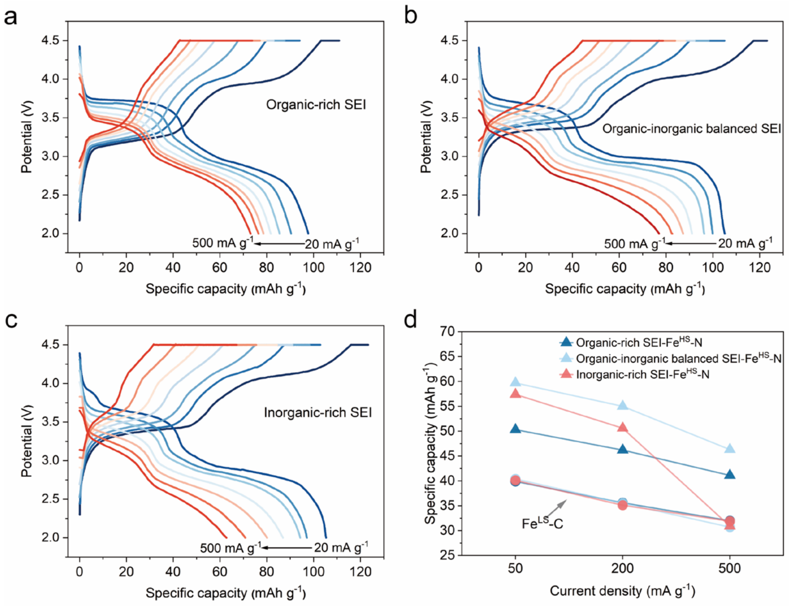

Figure S22 Charge-discharge curves of KFeHCF/Gr full cells at different current densities, cycled at 25°C: (a) Organic-rich SEI, (b) Organic-inorganic balanced SEI, (c) Inorganic-rich SEI, (d) Comparison of specific capacity.

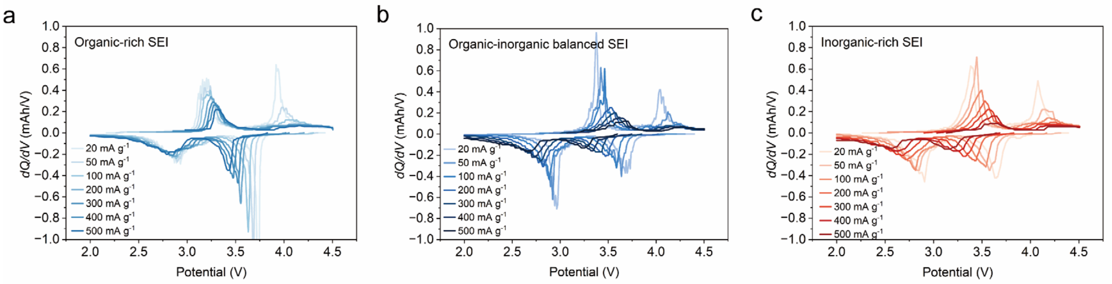

Figure S23. Differential capacity (d*Q*/d*V*) profiles of KFeHCF/Gr full cells at different current densities, cycled at 25°C: (a) Organic-rich SEI, (b) Organic-inorganic balanced SEI, (c) Inorganic-rich SEI.

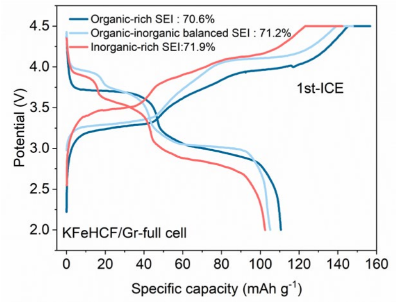

Figure S24. 1st curves of KFeHCF/Gr full cells at 20 mA g^{-1}.

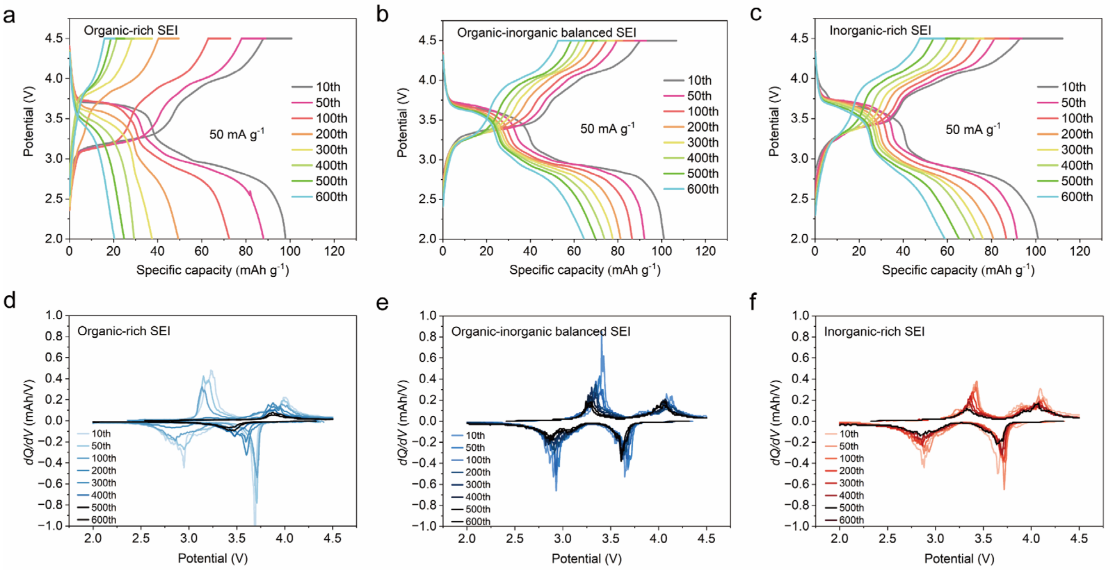

Figure S25. Charge-discharge curves of KFeHCF/Gr full cells at 50 mA g^{-1}: (a) Organic-rich SEI, (b) Organic-inorganic balanced SEI, (c) Inorganic-rich SEI. Differential capacity (d*Q*/d*V*) profiles of KFeHCF/Gr full cells at 50 mA g^{-1}: (d) Organic-rich SEI, (e) Organic-inorganic balanced SEI, (f) Inorganic-rich SEI.

Table S1 The comparison of Prussian Blue analogues/Graphite full-cell with other PIB full-cell systems in terms of specific capacity, rate performance, and cycling performance.

Cathode	Anode	Electrolyte	Specific capacity [mA h g^{-1}]	Rate performance [mA h g^{-1}]	cycling performance [%]
$K_2Fe[Fe(CN)_6]$ (this work)	graphite	0.8M KPF_6 in EC/DEC	105.1 at 20 mA g^{-1}	78 at 500 mA g^{-1}	71.6 (600 cycles, 50 mA g^{-1})
$K_2Fe[Fe(CN)_6]$[8]	graphite	0.8M KPF_6 in EC/DEC	94.3 at 50 mA g^{-1}	65.6 at 400 mA g^{-1}	77.33 (500 cycles, 50 mA g^{-1})
$K_2MnFe(CN)_6$ [9]	graphite	7M KFSI in DME	104 at 15 mA g^{-1}	/	85 (101 cycles, 150 mA g^{-1})
$K_2MnFe(CN)_6$ [10]	graphite	KFSI in ionic liquids	91 at 15 mA g^{-1}	/	76 (205 cycles, 150 mA g^{-1})
$K_2Ni_{0.5}Fe_{0.5}[Fe(CN)_6]$ [11]	graphite	1M KPF_6 in EC/DEC/PC	81.6 at 10 mA g^{-1}	53 at 500 mA g^{-1}	87.1 (500 cycles, 20 mA g^{-1})
$K_2Mn[Fe(CN)_6]$ [12]	graphite	2.6M KFSI in TEP	125 at 25 mA g^{-1}	88 at 625 mA g^{-1}	80 (1000 cycles, 62.5 mA g^{-1})
$K_{0.22}Fe[Fe(CN)_6]_{0.81}$ [13]	Super P	0.8M KPF_6 in EC/DEC	65 at 100 mA g^{-1}	/	93.4 (50 cycles, 100 mA g^{-1})
$K_{0.61}Fe[Fe(CN)_6]_{0.91}\cdot 0.32H_2O$ [14]	graphite	0.8M KPF_6 in EC/DMC	80.0 at 50 mA g^{-1}	/	100 (50 cycles, 50 mA g^{-1})

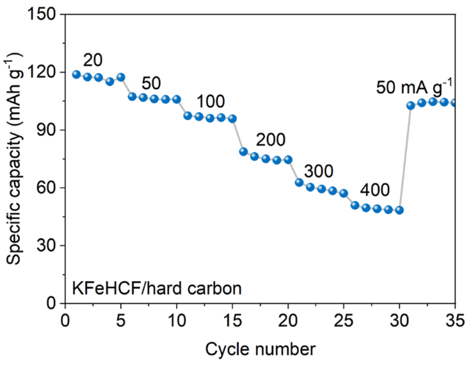

Figure S26. Cycling performance of KFeHCF/hard carbon full cell.

Supplementary Note 4:

Based on the study of KFeHCF/Gr full cell system, another anode material (hard carbon) has also been investigated to matchup with KFeHCF cathode. The hard carbon anode was pre-cycled at 25°C by using hard carbon/K half cell after 3 cycles and paired with pre-cycled KFeHCF cathode, then assembled to construct the full-cell. The as-prepared KFeHCF/hard carbon full cell shows good rate performance that can delivery 106.1 mAh g^{-1} specific capacity at current density of 50 mA g^{-1}, and nearly 62.7 mAh g^{-1} specific capacity at current density of 300 mA g^{-1} (**Figure S26**).

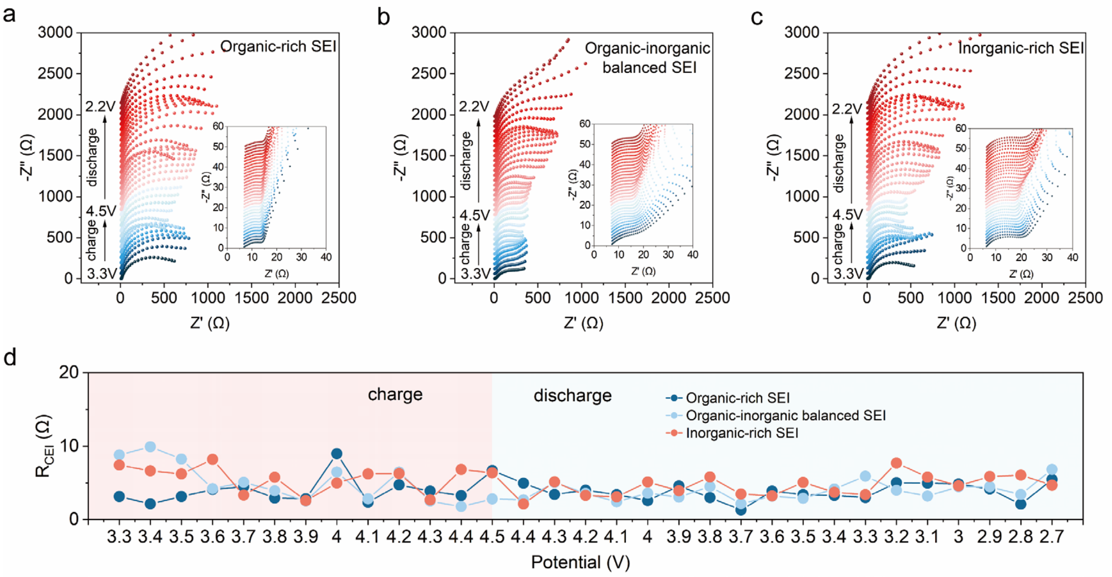

Figure S27. In situ EIS of KFeHCF/Gr full cells during first charge–discharge process: (a) Organic-rich SEI, (b) Organic-inorganic balanced SEI, (c) Inorganic-rich SEI, (d) Fitting impedance versus voltage profiles based on DRT results for R_{CEI}.

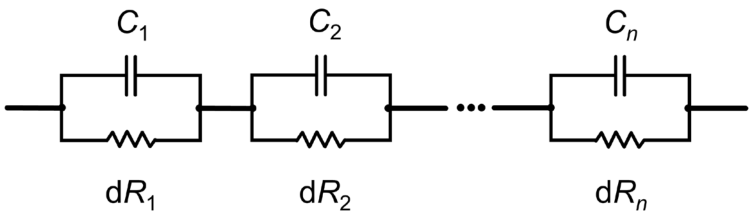

Figure S28. Voigt circuit model

Supplementary Note 5:

The characteristics of KFeHCF/Gr full cells are the result of a combined effect from both cathode and anode parts. However, the conventional experience-dependent equivalent circuit model (ECM) may lead to the misunderstanding in the battery analyses due to the similar time constants of electrochemistry processes of battery system.

To comprehensively analyze the kinetic processes, the distribution of relaxation times (DRT) is employed to transform EIS data from the frequency domain to the time domain. Based on the changes in DRT peaks and relaxation times (τ), the kinetic reaction processes of the full cell can be visually and accurately distinguished, thereby simplifying the analysis of impedance. In DRT analysis, the EIS is fitted with an infinite Voigt circuit, which consist of a series of resistors and constant phase elements (CPEs) in parallel (**Figure S28**). The transition relationship between frequency domain $Z(\omega)$ and time domain $\gamma(\tau)$ is displayed as[15]:

$$Z(\omega) = R_0 + Z_p(\omega) = R_0 + \int_0^{\infty} \frac{\gamma(\tau)}{1+j\omega\tau} d\tau \qquad (6)$$

Where $Z(\omega)$ is total impedance, R_0 is Ohm impedance, $Z_p(\omega)$ is polarization impedance, ω is frequency, and the polarization impedance is calculated as $\frac{\gamma(\tau)}{1+j\omega\tau} d\tau$.

Generally speaking, the properties of KFeHCF/Gr full cells are the superposition of both cathode and anode parts[16]. To assign the dominate processes in the DRT to their corresponding electrodes, the following experiments were systematically performed.

Firstly, the symmetrical potassium cells are constructed and their DRT curves are analyzed to investigate the impact of the K metal counter electrode on the half-cells.

Secondly, KFeHCF/K and Gr/K half cells are built by using pristine electrode and cycled to various state of charge (SOC), with their DRT curves are analyzed and compared with full cells.

In summary, the intrinsic reaction processes of the full cell can be precisely identified based on the corresponding relaxation time ranges and trends of DRT peak intensities, according to our previous work[8]. The response times of four kinetic processes within the full cell, ordered from high to low relaxation time, are associated with the anodic charge transfer, cathodic charge transfer, K^+ crossing SEI, and K^+ crossing CEI.

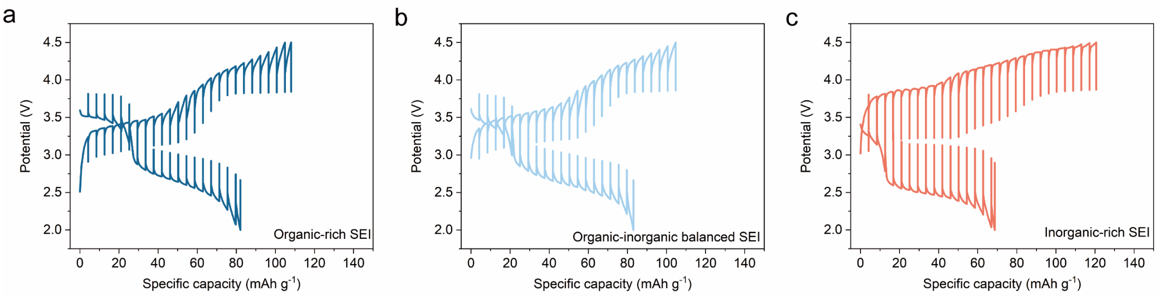

Figure S29. GITT curves of KFeHCF/Gr full cells during charge−discharge process: (a) Organic-rich SEI, (b) Organic-inorganic balanced SEI, (c) Inorganic-rich SEI.

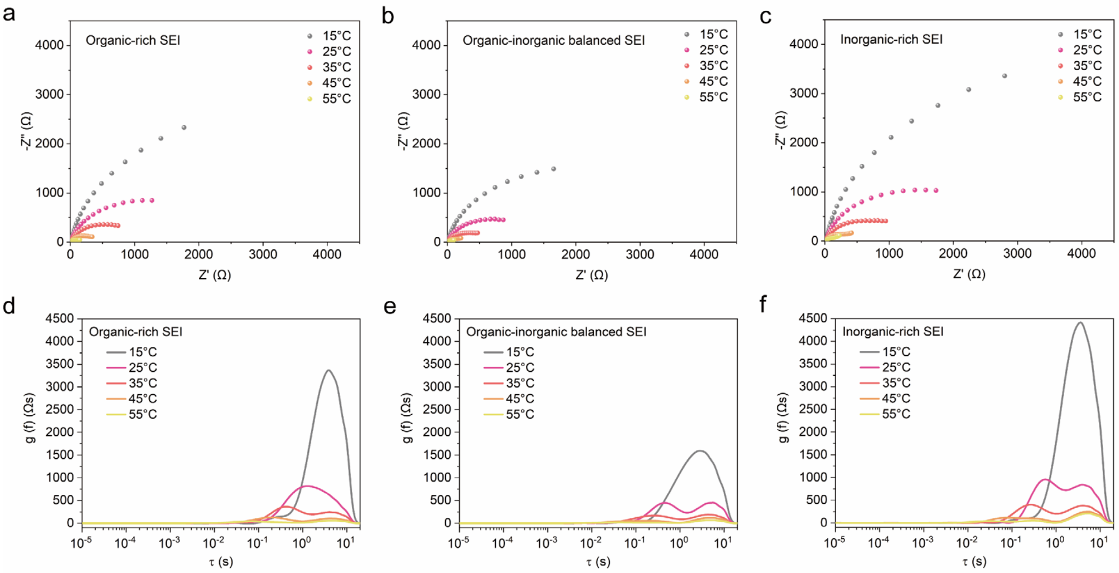

Figure S30. Nyquist impedance spectroscopy at a KFeHCF/Gr full cell voltage of 4.5 V in different temperatures (15, 25, 35, 45ºC, 55ºC the absolute temperature are 288.15, 298.15, 308.15, 318.15 K, 328.15 K, respectively): (a) Organic-rich SEI, (b) Organic-inorganic balanced SEI, (c) Inorganic-rich SEI. The corresponding DRT results: (d) Organic-rich SEI, (e) Organic-inorganic balanced SEI, (f) Inorganic-rich SEI.

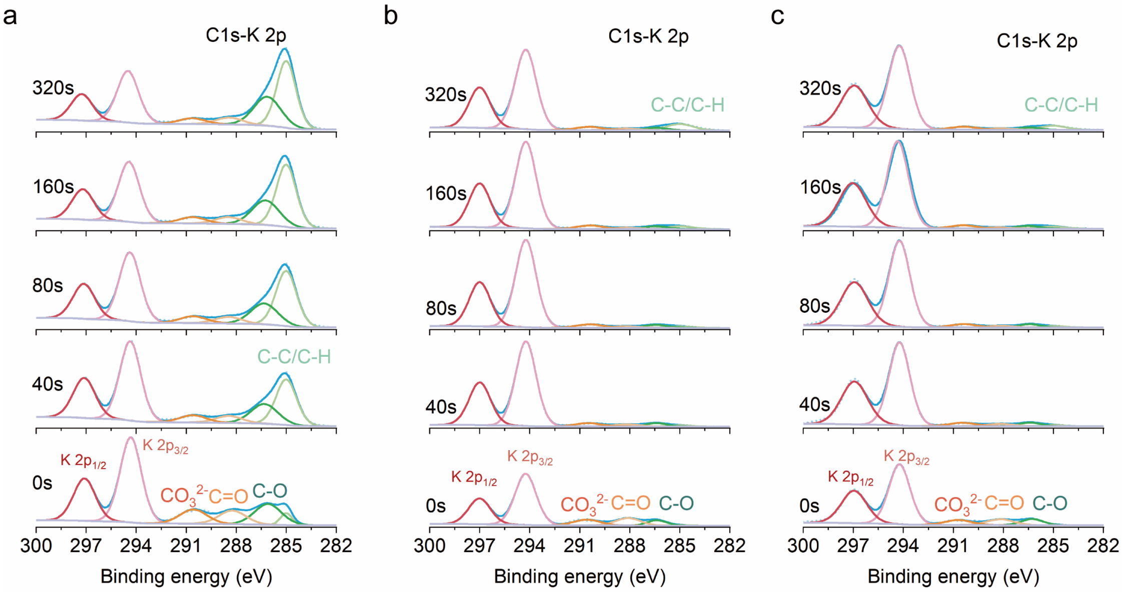

Figure S31. Comparative C 1s-K 2p spectra analysis of the Gr anode retrieved from KFeHCF/Gr full cell after 3 cycles with (a) Organic-rich SEI, (b) Organic-inorganic balanced SEI, (c) Inorganic-rich SEI.

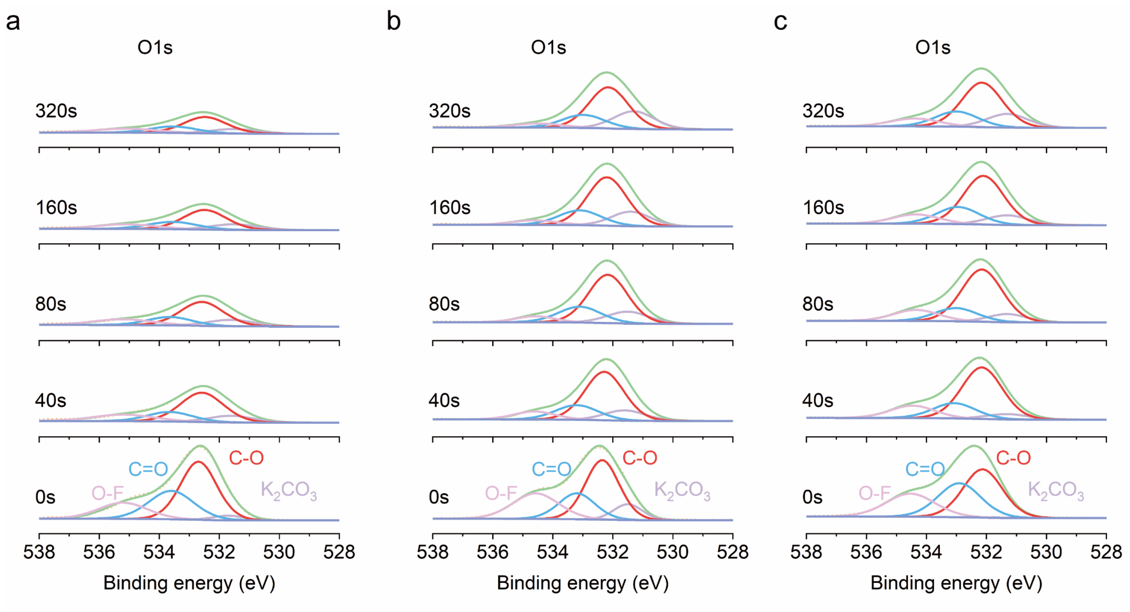

Figure S32. Comparative O 1s spectra analysis of the Gr anode retrieved from KFeHCF/Gr full cell after 3 cycles with (a) Organic-rich SEI, (b) Organic-inorganic balanced SEI, (c) Inorganic-rich SEI.

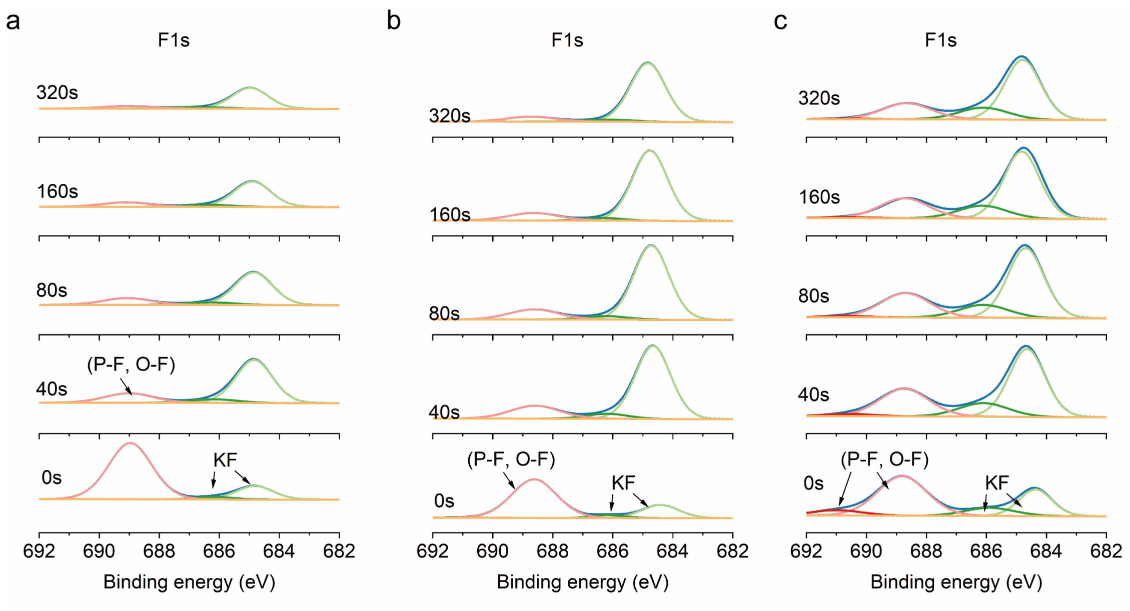

Figure S33. Comparative F 1s spectra analysis of the Gr anode retrieved from KFeHCF/Gr full cell after 3 cycles with (a) Organic-rich SEI, (b) Organic-inorganic balanced SEI, (c) Inorganic-rich SEI.

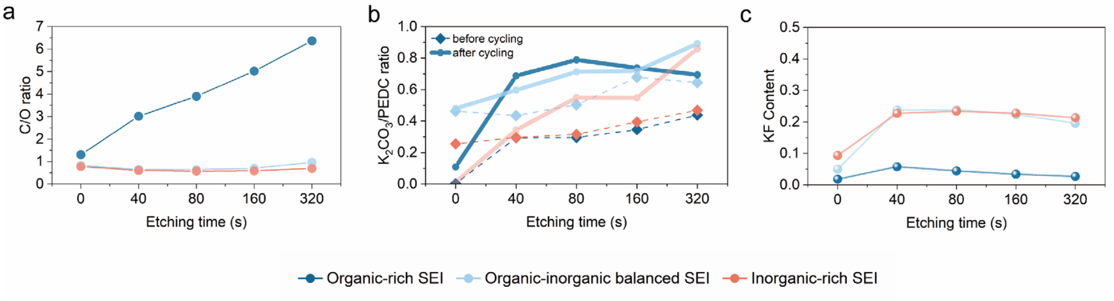

Figure S34. Depth profiling XPS analysis of the SEI chemistry retrieved from KFeHCF/Gr full cells after 3 cycles, with sputtering time 0 and 320 s: (a) Relative atomic ratios of C/O, (b) K_2CO_3 to PEDC ratio in SEI based on O 1s spectra, (c) KF content.

References

1. M. Ye, S. You, J. Xiong, Y. Yang, Y. Zhang and C. C. Li, *Mater. Today Energy*, 2022, **23**, 100898-100906.
2. J. Zhang, J. Wu, Z. Wang, Y. Mo, W. Zhou, Y. Peng, B. He, K. Xiao, S. Chen, C. Xu and J. Liu, *J. Energy Chem.*, 2022, **71**, 344-350.
3. J.-F. Ding, R. Xu, C. Yan, B.-Q. Li, H. Yuan and J.-Q. Huang, *J. Energy Chem.*, 2021, **59**, 306-319.
4. L. Ni, G. Xu, C. Li and G. Cui, *Exploration*, 2022, **2**, 20210239.
5. W. Zhou, B. He, L. Quan, R. Li, Y. Chen, C. Fan, S. Chen, C. Xu, X. Fan, L. Xing and J. Liu, *Adv. Energy Mater.*, 2023, **13**, 2202874.
6. J. C. Chacón-Torres and T. Pichler, *Physica Status Solidi (B)*, 2011, **248**, 2744-2747.
7. W. Luo, J. Wan, B. Ozdemir, W. Bao, Y. Chen, J. Dai, H. Lin, Y. Xu, F. Gu, V. Barone and L. Hu, *Nano Lett.*, 2015, **15**, 7671-7677.
8. Y. Mo, W. Zhou, K. Wang, K. Xiao, Y. Chen, Z. Wang, P. Tang, P. Xiao, Y. Gong, S. Chen, P. Gao and J. Liu, *ACS Energy Lett.*, 2023, **8**, 995-1002.
9. T. Hosaka, K. Kubota, H. Kojima and S. Komaba, *Chemical Communications*, 2018, **54**, 8387-8390.
10. H. Onuma, K. Kubota, S. Muratsubaki, T. Hosaka, R. Tatara, T. Yamamoto, K. Matsumoto, T. Nohira, R. Hagiwara, H. Oji, S. Yasuno and S. Komaba, *ACS Energy Lett.*, 2020, **5**, 2849-2857.
11. S. Chong, J. Yang, L. Sun, S. Guo, Y. Liu and H. K. Liu, *ACS Nano*, 2020, **14**, 9807-9818.
12. X. Wu, S. Qiu, Y. Liu, Y. Xu, Z. Jian, J. Yang, X. Ji and J. Liu, *Adv. Mater.*, 2022, **34**, e2106876-e2106885.
13. C. Zhang, Y. Xu, M. Zhou, L. Liang, H. Dong, M. Wu, Y. Yang and Y. Lei, *Adv. Funct. Mater.*, 2017, **27**, 1604307-1604314.
14. Y.-H. Zhu, X. Yang, D. Bao, X.-F. Bie, T. Sun, S. Wang, Y.-S. Jiang, X.-B. Zhang, J.-M. Yan and Q. Jiang, *Joule*, 2018, **2**, 736-746.
15. Y. Lu, C.-Z. Zhao, J.-Q. Huang and Q. Zhang, *Joule*, 2022, **6**, 1172-1198.
16. P. Shafiei Sabet and D. U. Sauer, *J. Power Sources*, 2019, **425**, 121-129.